Supporting Information

Contrasting Impacts of Policy Interventions and Population Mobility on Organic Aerosols and Oxygenated Volatile Organic Compounds in Beijing

Yu Zhang[1,2,3], Weiqi Xu[1] *, Wei Zhou[1], Jintai Lin[4], Mengying Wang[4], Yan Li[1], Siqi Zeng[1,2], Ziyi Zhang[2,5], Xiaomin Cheng[1,2], Yang Yang[3,6], Yele Sun[1,2]

[1]*State Key Laboratory of Atmospheric Environment and Extreme Meteorology, Institute of Atmospheric Physics, Chinese Academy of Sciences, Beijing 100029, China*

[2]*College of Earth and Planetary Sciences, University of Chinese Academy of Sciences, Beijing 100049, China*

[3]*Hebei Provincial Weather Modification Center, Shijiazhuang, 050021, China*

[4]*Laboratory for Climate and Ocean–Atmosphere Studies, Department of Atmospheric and Oceanic Sciences, School of Physics, Peking University, Beijing 100871, China.*

[5]*State Key Laboratory of Earth System Numerical Modeling and Application, Institute of Atmospheric Physics, Chinese Academy of Sciences, Beijing 100029, China*

[6]*Key Laboratory of Meteorology and Ecological Environment of Hebei Province, Shijiazhuang, 050021, China*

*Corresponding Author: Weiqi Xu (xuweiqi@mail.iap.ac.cn)

List of the supporting information:

Text S1 PMF analysis of organic aerosols 1
Text S2 Source Apportionment Using the ME-2 Model 2
Text S3 PMF^2 analysis of volatile organic compounds and OA 2
Text S4 Saturation Concentration Calculation and Volatility Classification 4
Figure S1. The correlation between NR-PM (measured by the ACSM/AMS)+BC and $PM_{2.5}$ from the Olympic Sports Center station for each year, with Slope and R^2 values indicated. 5
Figure S2. High-resolution mass spectra (left panel) and time series (right panel) of the mass concentration of 4-factor and 6-factor solution resolved by PMF. The panel below shows the time series of the mass concentration of factor 1st for 5-factor solution and the sum of factor 1st and 2nd for 6-factor solution. 6
Figure S3. High-resolution (a) mass spectra of 5-factor solution resolved by PMF, and time series of the mass concentration in (b)2021 and (c)2022. 7
Figure S4. Correlations of five OA factors with external tracers in 2021 and 2022. Also shown are the diurnal variations of mass concentrations and fractions of non- refractory particulate matter (NR-PM) species and OA factors in 2021 and 2022. 8
Figure S5. Temporal variations and mass spectra of five factors from bootstrapping analysis (100 iterations) for PMF. The error bar is the standard deviation. 9
Figure S6. Comparison of OA factors from two analyses. Time series from the ambient $PMF_{2021+2022}$ (black) versus the constrained ME-2 analysis (a-value = 0.3) applied to the combined dataset of ambient and OFR-aged aerosols from 2022 (red lines). 10
Figure S7. Mass spectra of 8-factor, 7-factor and 9-factor solution determined by the PMF^2 model. The bar plots (left y-axis) depict the mass spectral profiles of the eight resolved factors, note that the VOC mass spectra are not displayed in this figure. The pink dots (right y-axis) represent the relative contribution of each individual factor to the different chemical components on the x-axis, where the contributions of all eight factors to any given component sum to 100%. 11
Figure S8. Time series of the 8-factor solution resolved by the PMF^2 model for 2021 and 2022. 12
Figure S9. Temporal variations and mass spectra of eight factors from bootstrapping analysis (100 iterations) for PMF^2. The error bar is the standard deviation. 13
Figure S10. Correlation between results predicted by the Random Forest (RF) algorithm and observations. 14
Figure S11. Spatial distribution of tropospheric nitrogen dioxide vertical column densities (NO_2 VCDs) change rates (%) over the North China Plain. Results are derived from POMINO-OMI satellite retrievals and represent three policy interventions ($APEC_{2014}$, $V\text{-}Day_{2015}$, WOG_{2022}) and three Chinese New Year ($CNY_{2019\text{-}2021}$). Blue hues indicate decreases in NO_2 VCDs, while red hues represent increases. 16
Figure S12. Average size distributions of sulfate, nitrate, and organics measured during emission variation and non-emission variation periods for regional coordinated emission reduction scenarios ($APEC_{2014}$, $V\text{-}Day_{2015}$, WOG_{2022}), also shown are the percentage changes in their mass concentrations across different size ranges. 16
Figure S13. Signal fraction of VOC components at each saturation concentration before

and during the Winter Olympic Games (BWOG and WOG). 17
Figure S14. Mass concentrations of the three SOA factors in (a) 2021–2022, (b) BWOG–WOG, and signal intensities of CHO (orange) and CHON (green) compounds contributing to each factor. 17
Figure S15. Absolute change of elemental ratios of OA as a function of photochemical age for BWOG, WOG, and entire period in 2022. 18
Figure S16. Time series of (a) relative humidity (RH) and temperature (*T*), mass concentrations of (b) OA factor and (c) NR-PM species in 2022. The shading area indicates WOG. Ep1 and Ep2 represent two pollution episodes and C1–C2 represent two cleaning episodes. 19
Figure S17. VOC mass spectra and relative changes between Ep1 and Ep2 Periods. Percentage reduction of individual VOC signals from Ep1 to Ep2 is calculated as (Ep1-Ep2)/Ep1×100%. Only positive values (indicating a reduction during Ep2) are displayed. Specific compounds with reductions exceeding 50% are labeled. 20
Figure S18. Absolute and relative enhancements of the mass concentration of OA as a function of photochemical age for C1 and C2 cleaning episodes. 21
Table S1. Overview of measurement campaigns, instrumentation, and defined analysis periods. 22
Table S2. Collection efficiency (CE) and relative ionization efficiency (RIE) used in 2014–2022 23
Table S3. A summary of the OH exposure, eq. photochemical age, ozone (O_3) levels and O_3/OH_{exp} ratio for the different light intensities in the OFR reactor. 23
Table S4. Performance metrics of the random forest model used for meteorological normalization, including the root mean square error (RMSE) and mean absolute error (MAE) for each species and year. 24
Table S5. A summary of average mass concentrations of gaseous pollutants and particulate matter components measured during the emission variation and non-emission variation period for policy interventions ($APEC_{2014}$, $V\text{-}Day_{2015}$, WOG_{2022}) and population mobility ($CNY_{2019\text{-}2021}$). 25
Table S6. Summary of key VOCs identified in this study, including their molecular formulas, proposed identities, and supporting references. 26
Table S7. A summary of average signal intensities and signal fractions of different VOC components for WOG_{2022} and the same period in 2021, BWOG, WOG , and Ep1, Ep2 pollution episodes, C1, C2 cleaning episodes in WOG_{2022} 27
References 29

Text S1 PMF analysis of organic aerosols

To facilitate a comparative analysis of actual atmospheric conditions in 2021 and 2022, organic aerosol (OA) data were combined and subjected to joint positive matrix factorization (PMF) source apportionment($PMF_{2021+2022}$). As shown in Figure S2, the 4-factor solution by PMF yielded a mixed factor (Factor 4), characterized by prominent signals of both CH and CHO fragments, indicating a mixture of primary organic aerosol (POA) and secondary organic aerosol (SOA). In the 6-factor solution (Figure S2), one SOA factor was split into two, whose mass spectra and time series were highly similar. Moreover, the summed time series of these two factors closely matched that of the first factor in the 5-factor solution. Therefore, the five-factor solution (Figure S3) was selected for subsequent analysis.

The mass spectrum of non-cooking OA (nCOA) exhibits prominent signals from hydrocarbon fragments ($C_nH_{2n+1}^+$, $C_nH_{2n-1}^+$), along with a distinct peak at *m/z* 115, which is likely associated with aromatic species. Additionally, strong biomass burning markers are observed at *m/z* 60 and 73, with f_{60}=1.2%, f_{73}=0.7% (f_{60} and f_{73} represent the fractional contributions of *m/z* 60 and 73 to total OA, respectively) (Figure S4). These characteristics indicate that nCOA is a mixture of biomass-burning organic aerosol (BBOA) (Cubison et al., 2011) and fossil fuel combustion organic aerosol (FFOA) (Sun et al., 2016). The COA mass spectrum displays a relatively high f_{55}/f_{57} ratio (2.4) and clear diurnal variation, with two distinct peaks during lunchtime and evening meal times, corresponding to cooking activities. Therefore, it is defined as a cooking-related factor. Similar to previous studies (Sun et al., 2013), the three SOA factors show strong signals at *m/z* 44 and *m/z* 43, and exhibited high correlations with secondary inorganic aerosols (SIA) (Figure S4) (Fröhlich et al., 2015). Specifically, oxidized primary OA (OPOA) showed a high oxygen-to-carbon ratio (O/C = 0.90), along with elevated f_{43} (7.9%) and f_{44} (18.2%), consistent with typical features of secondary aerosols. Its strong correlation with black carbon (BC) (R^2=0.8-0.9) suggests that it likely represents a secondary factor formed through the oxidation of primary emissions. Oxidized OA (OOA1) exhibited a clear diurnal pattern, indicating a close association with photochemical aging processes. In contrast, OOA2 had a higher O/C ratio than OOA1 (0.92 vs. 0.69), but it did not shown obvious diurnal variation (Figure

S4), suggesting that it may represent more aged organic aerosols, likely influenced by regionally transported air masses.

Text S2 Source Apportionment Using the ME-2 Model

To ensure that the organic aerosol factors resolved from the 2022 dataset incorporating OFR aging were directly comparable with those obtained from the combined 2021 and 2022 bypass data, source apportionment was further conducted using the Multilinear Engine-2 (ME-2) algorithm. The ME-2 approach is based on PMF principles but allows for the introduction of known factor profiles as constraints, providing additional control over the rotational ambiguity inherent in the model (Paatero and Hopke, 2009).

Specifically, the mass spectral profiles of the five OA factors (namely nCOA, COA, OPOA, OOA1, and OOA2) identified from the previous combined PMF analysis of the 2021 and 2022 bypass data were used as prior information (constraints) for the ME-2 analysis of the combined 2022 bypass and OFR dataset. The strength of these constraints was controlled using the a-value parameter, which defines the allowable range of variation for the constrained factor profiles from their initial spectra (Lanz et al., 2007). In this analysis, the a-value was set to vary from 0 to 1 at intervals of 0.1 during the solution exploration.

The solution obtained with an a-value of 0.3 was selected for this study. The factor profiles and their time series derived from this ME-2 analysis showed strong correlations and were nearly identical to those from the combined PMF analysis of the 2021 and 2022 bypass data (Figure S6). All ME-2 calculations were performed using the Source Finder (SoFi) tool (Canonaco et al., 2013) based on the Igor Pro environment.

Text S3 PMF^2 analysis of volatile organic compounds and OA

To evaluate the contribution of volatile organic compounds (VOCs) on particulate matter, particularly SOA, we combined the mass concentration matrices of particulate matter and OA factors (including OOA1, OOA2, OPOA, COA, and nCOA, as detailed in Text S1) with the VOC signals matrix, and all variables were then normalized to their respective maximum values to eliminate the influence of differing units from particles and VOCs. Then a second positive matrix factorization (PMF^2) analysis was subsequently conducted. The error matrix was determined using the following equation:

$$U_{ij}=\begin{cases} \frac{5}{6}LOD_i & if\ C_{i,j}\leq LOD_i \\ \sqrt{u_i^2C_{i,j}^2+LOD_i^2} & if\ C_{i,j}\geq LOD_i \end{cases}$$

Here, C represents the number of species, LOD is the limit of detection, and u denotes the relative uncertainty of each variable (expressed as a percentage). $u_{i,j}$ represents the final uncertainty for species i in row j, which is determined by the LOD and u. More detailed descriptions, as well as specific parameters for particulate matter and OA factors, can be found in previous studies (Petit et al., 2014). For VOCs, $u_{i,j}$ was uniformly set to 15%, and the LOD was defined as three times the standard deviation of the background signal.

Figure S7 presents the mass spectral profiles and relative source contributions for the PMF^2 solution. The pink dots (right y-axis) quantify the relative contribution of each individual factor to the different chemical components on the x-axis, it should be noted that the information of VOCs is omitted in the spectrum. In the 7-factor solution, Factor 7 contributed 58.1% and 37.8% to COA and nCOA, respectively, and it was also the main contributor to OOA1, accounting for as much as 87.7% of OOA1, much higher than the other factors, indicating that this factor contributes to both POA and SOA, may be a mixed factor. In the 8-factor solution, Factor 8 was the main contributor to OOA1 (85.2%), similar to Factor 7 in the 7-factor solution, but its contribution to COA and nCOA decreased to 43.4% and 34.5%, respectively. This indicates that, compared with the 7-factor solution, the 8-factor result more clearly separated the POA-related and SOA-related factors. In the 9-factor solution, factor 9 exhibited characteristics similar to Factor 8 in the 8-factor result, with respective contributions of 39.0%, 33.1%, and 82.1% to COA, nCOA, and OOA1, suggesting that increasing the number of factors did not significantly improve the separation between POA-related and SOA-related factors. Therefore, the 8-factor solution was selected as the optimal result (Figure S7). Factor 8, Factor 5, and Factor 4 were identified as the factors associated with OOA1, OOA2, and OPOA, respectively, each making the highest relative contribution to their corresponding SOA factors (85.2%, 60.0%, and 55.7%). It is worth noting, however, that some uncertainties remain in this solution. For example, Factor 8 still contributed

23.1% to OOA2, Factor 4 and 7 also contributed partially to OPOA (26.4% and 12.1%, respectively), reflecting incomplete separation of POA-related and SOA-related signals, thereby potentially affecting the accuracy of subsequent source apportionment. Factor 7 makes certain contributions to POA (approximately 40%), it may be a mixed factor or related to some sources of POA. The contributions of Factor 1, Factor 2, Factor 3 and Factor 6 to all OA components were extremely low, indicating that they were secondary or background factors. It has no strong correlation with the main primary and secondary OA sources. The temporal trends of the eight factors are shown in Figure S8. The results indicate that the time series of Factor 8, Factor 5, and Factor 4 are similar to those of OOA1, OOA2, and OPOA, respectively. As normalized concentrations were introduced into the model, their concentration ranges do not exceed 1.

Text S4 Saturation Concentration Calculation and Volatility Classification

The saturation concentration (C_0) is a key thermodynamic parameter for assessing the volatility of organic compounds. Its calculation method can be found in the study by Li et al. (2016) Based on an elemental composition parameterization scheme, C_0 can be estimated using the following equation:

$$log_{10}C_0=\left(n_C^0-n_C\right)b_C-n_Ob_O-2\frac{n_Cn_O}{n_C+n_O}b_{CO}-n_Nb_N$$

Here, n_C, n_O, and n_N represent the number of carbon, oxygen, and nitrogen atoms, respectively. b_C, b_O, and b_N denote the contributions of each atom to $\log_{10}C_0$, while b_{CO} accounts for the carbon-oxygen non-ideality coefficient. For CHO-VOCs, the parameters n_C^0, b_C, b_O, and b_{CO} are set to 22.66, 0.4481, 1.656, and -0.7790, respectively. For CHON-VOCs, n_C^0, b_C, b_O, b_{CO}, and b_N are set to 24.13, 0.3667, 0.7732, -0.07790, and 1.114, respectively. Further details on these empirical coefficients and the calculation procedures can be found in Li et al. (2016).

According to the method proposed by Donahue et al. (2006) , organic compounds can be classified based on their saturation concentration. Specifically, semi-volatile organic compounds (SVOCs) have a $\log_{10}C_0$ range of -0.3 to 2.7 μg m^{-3}, while intermediate-volatility organic compounds (IVOCs) and VOC fall within the ranges of 2.7–6.7 μg m^{-3} and above 6.7 μg m^{-3}, respectively.

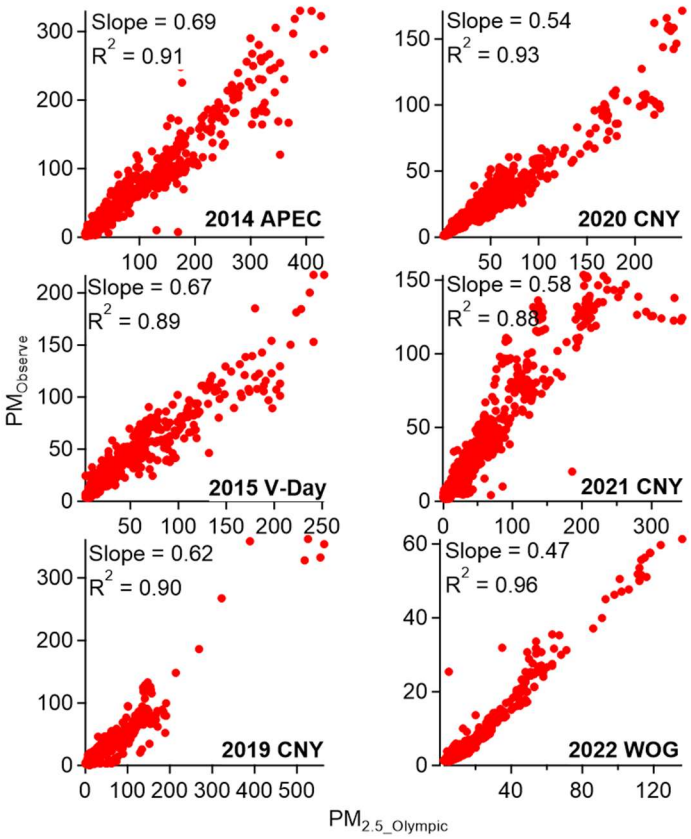


Figure S1. The correlation between NR-PM (measured by the ACSM/AMS)+BC and $PM_{2.5}$ from the Olympic Sports Center station for each year, with Slope and R^2 values indicated.

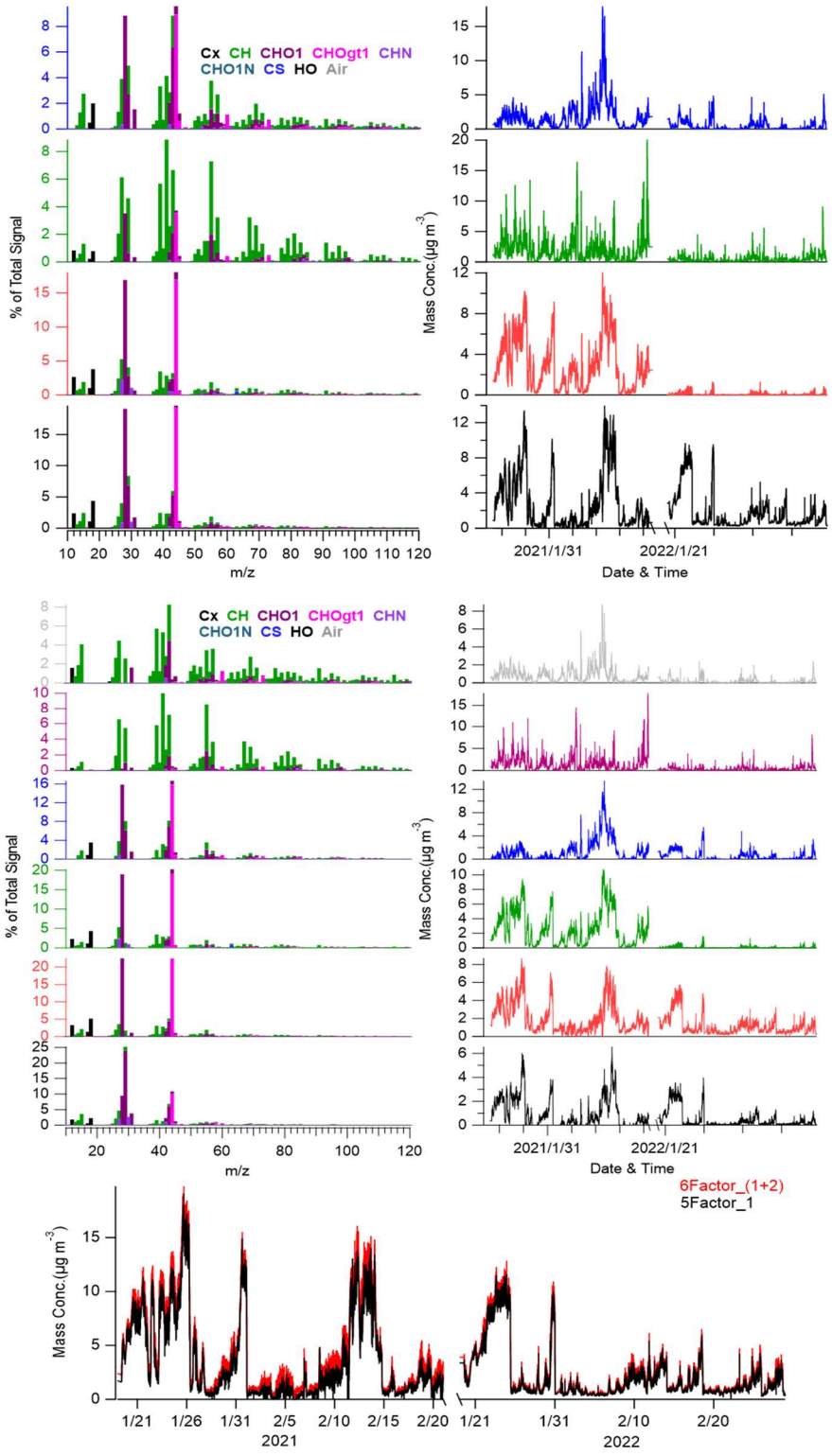


Figure S2. High-resolution mass spectra (left panel) and time series (right panel) of the mass concentration of 4-factor and 6-factor solution resolved by PMF. The panel below shows the time series of the mass concentration of factor 1st for 5-factor solution and the sum of factor 1st and 2nd for 6-factor solution.

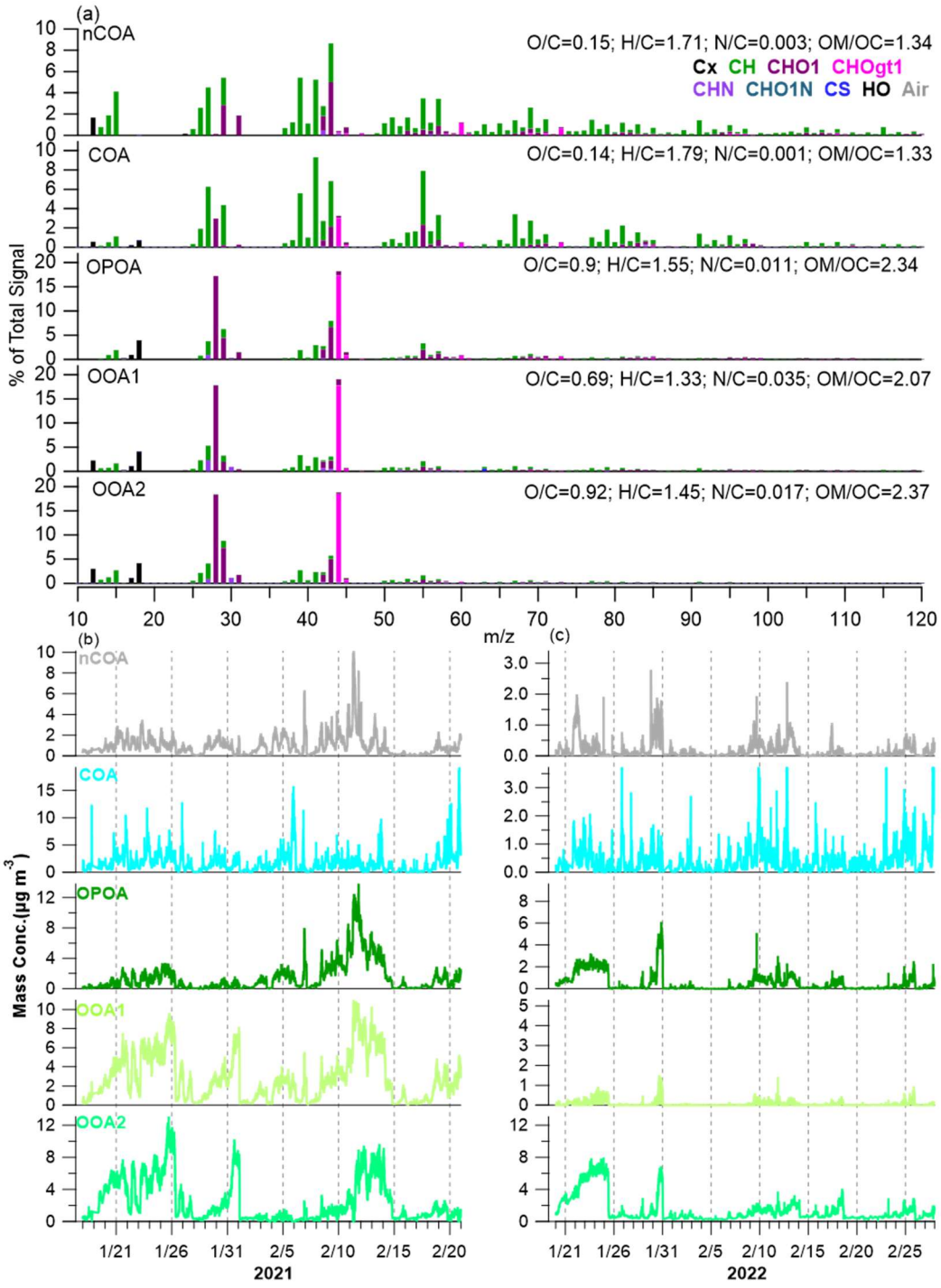


Figure S3. High-resolution (a) mass spectra of 5-factor solution resolved by PMF, and time series of the mass concentration in (b)2021 and (c)2022.

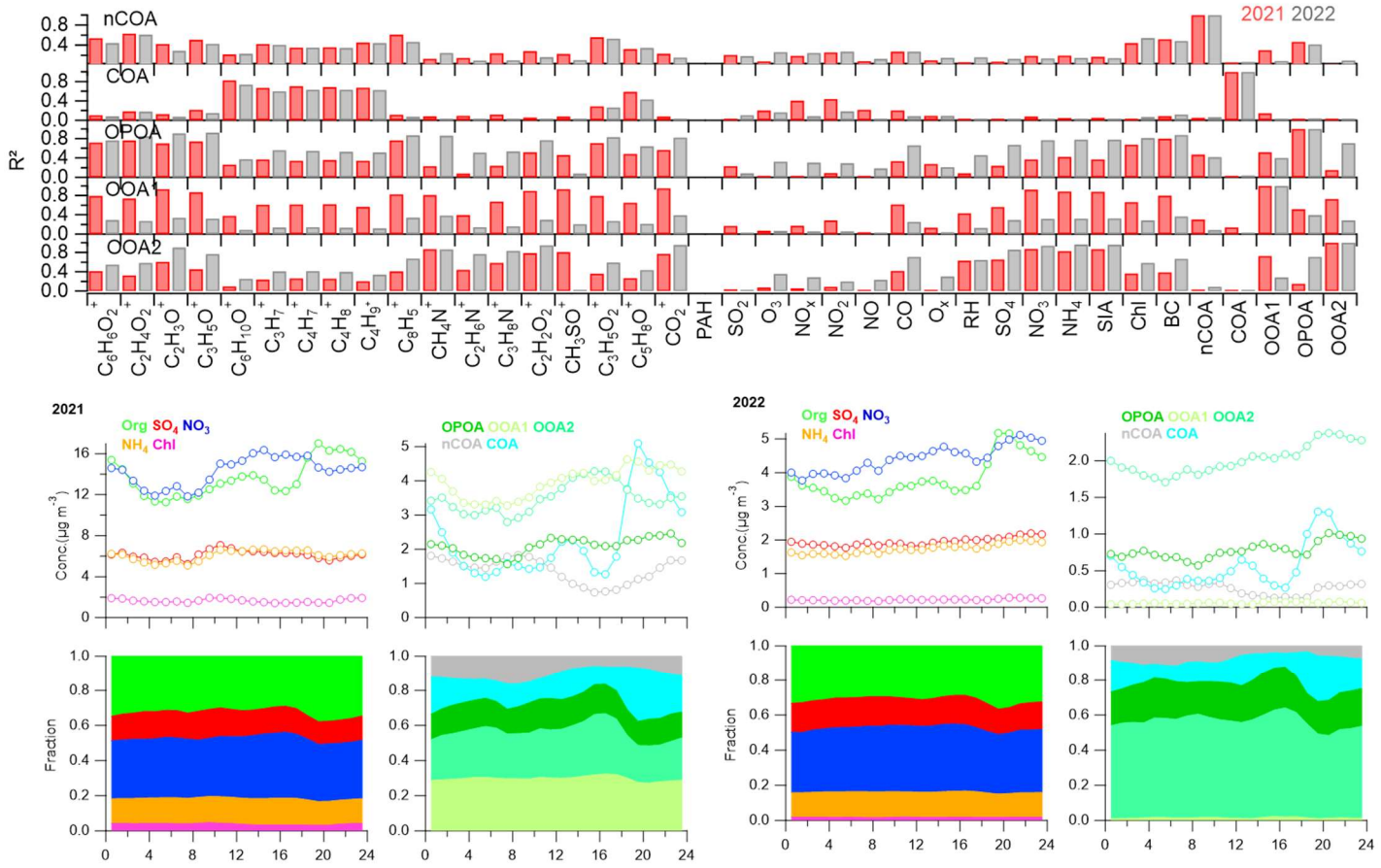


Figure S4. Correlations of five OA factors with external tracers in 2021 and 2022. Also shown are the diurnal variations of mass concentrations and fractions of non- refractory particulate matter (NR-PM) species and OA factors in 2021 and 2022.

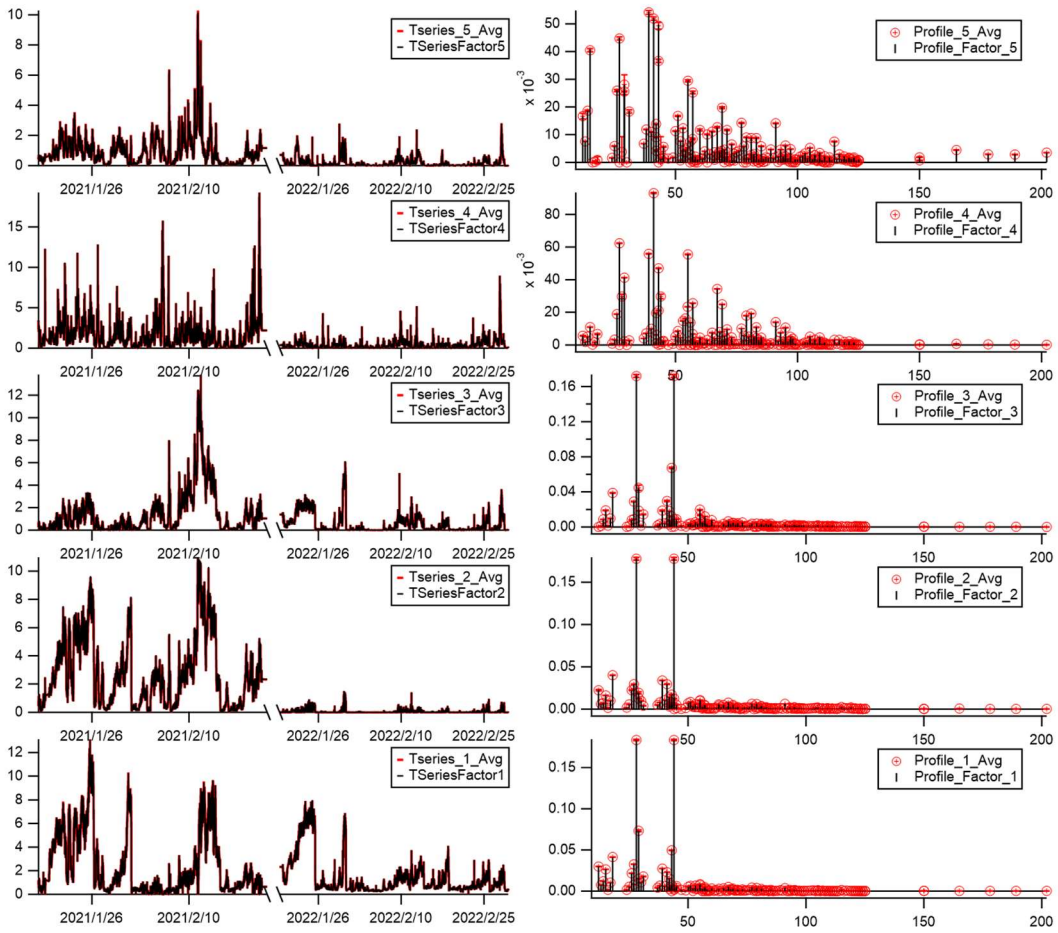


Figure S5. Temporal variations and mass spectra of five factors from bootstrapping analysis (100 iterations) for PMF. The error bar is the standard deviation.

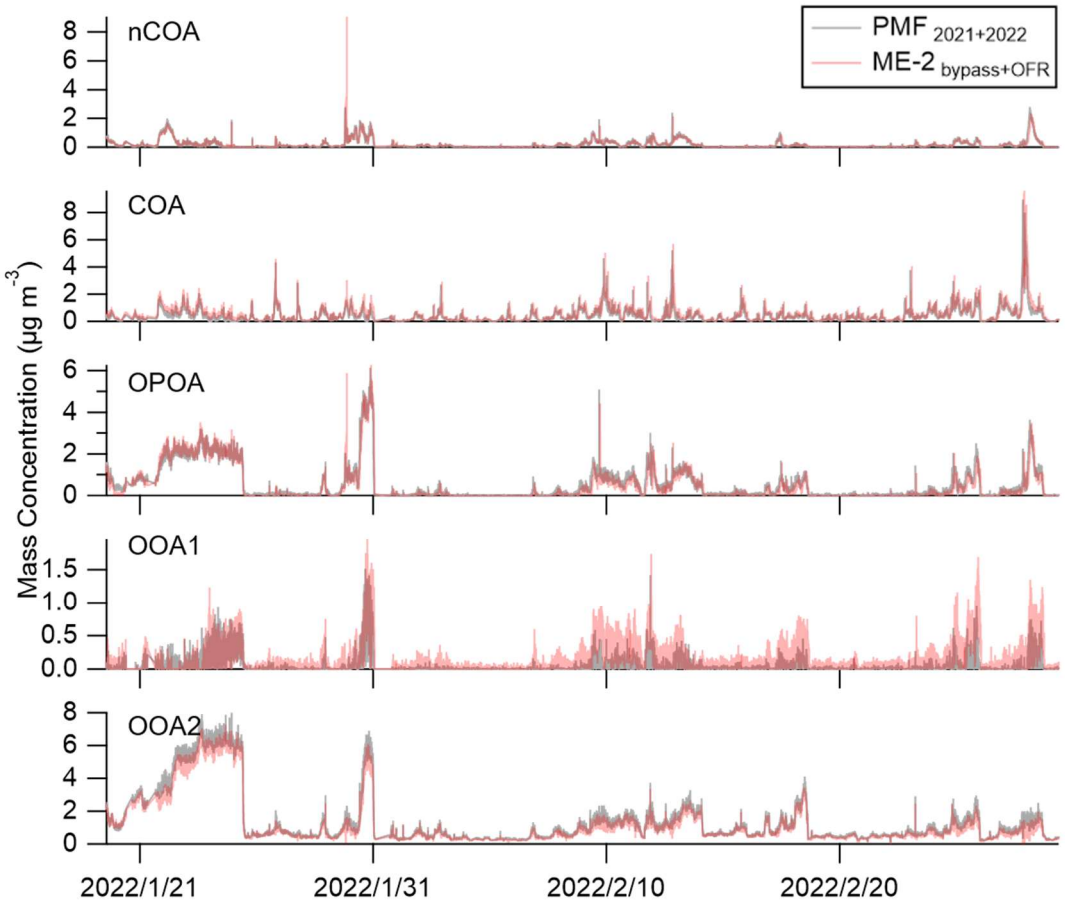


Figure S6. Comparison of OA factors from two analyses. Time series from the ambient $PMF_{2021+2022}$ (black) versus the constrained ME-2 analysis (a-value = 0.3) applied to the combined dataset of ambient and OFR-aged aerosols from 2022 (red lines).

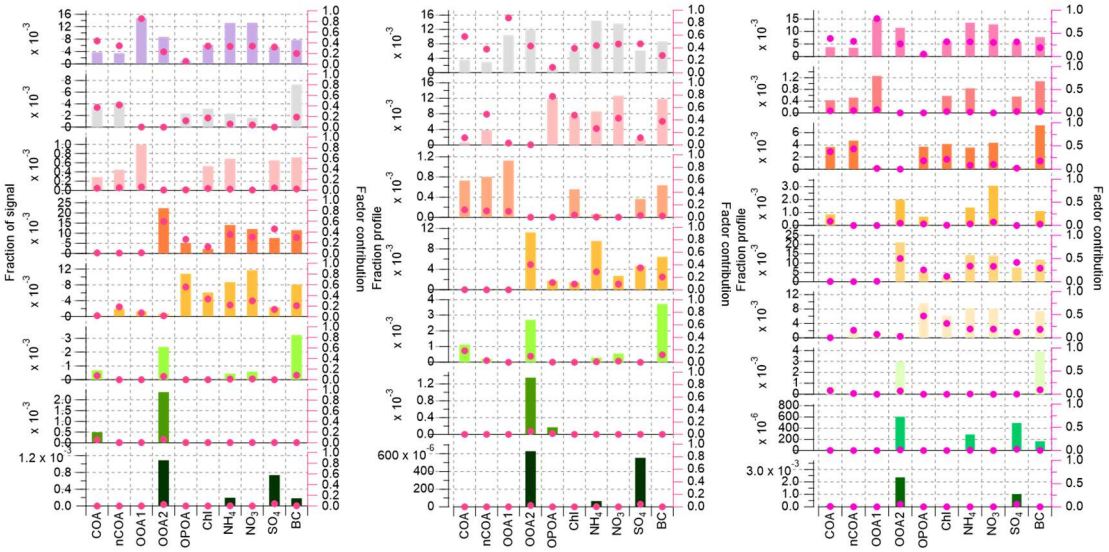


Figure S7. Mass spectra of 8-factor, 7-factor and 9-factor solution determined by the PMF^2 model. The bar plots (left y-axis) depict the mass spectral profiles of the eight resolved factors, note that the VOC mass spectra are not displayed in this figure. The pink dots (right y-axis) represent the relative contribution of each individual factor to the different chemical components on the x-axis, where the contributions of all eight factors to any given component sum to 100%.

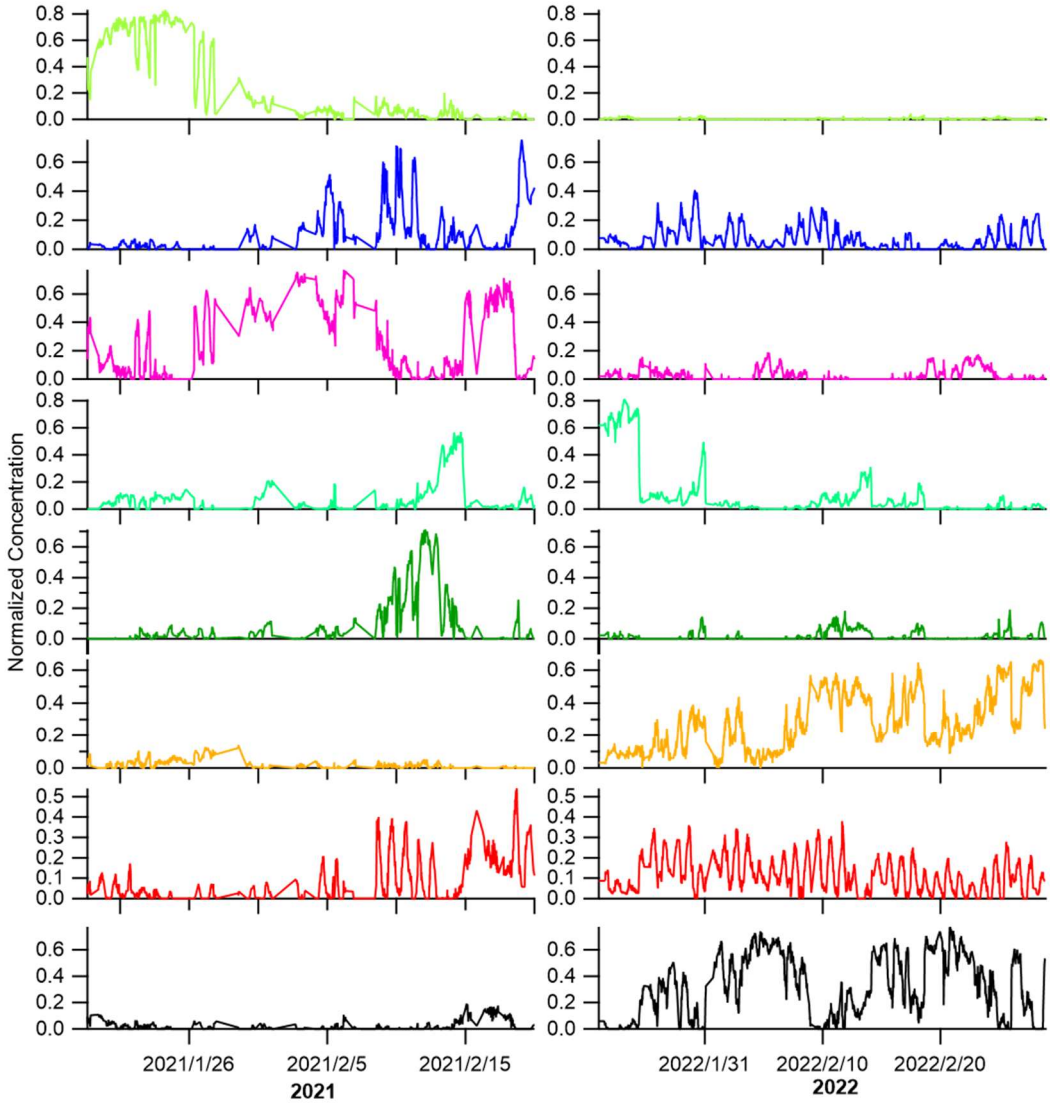


Figure S8. Time series of the 8-factor solution resolved by the PMF^2 model for 2021 and 2022.

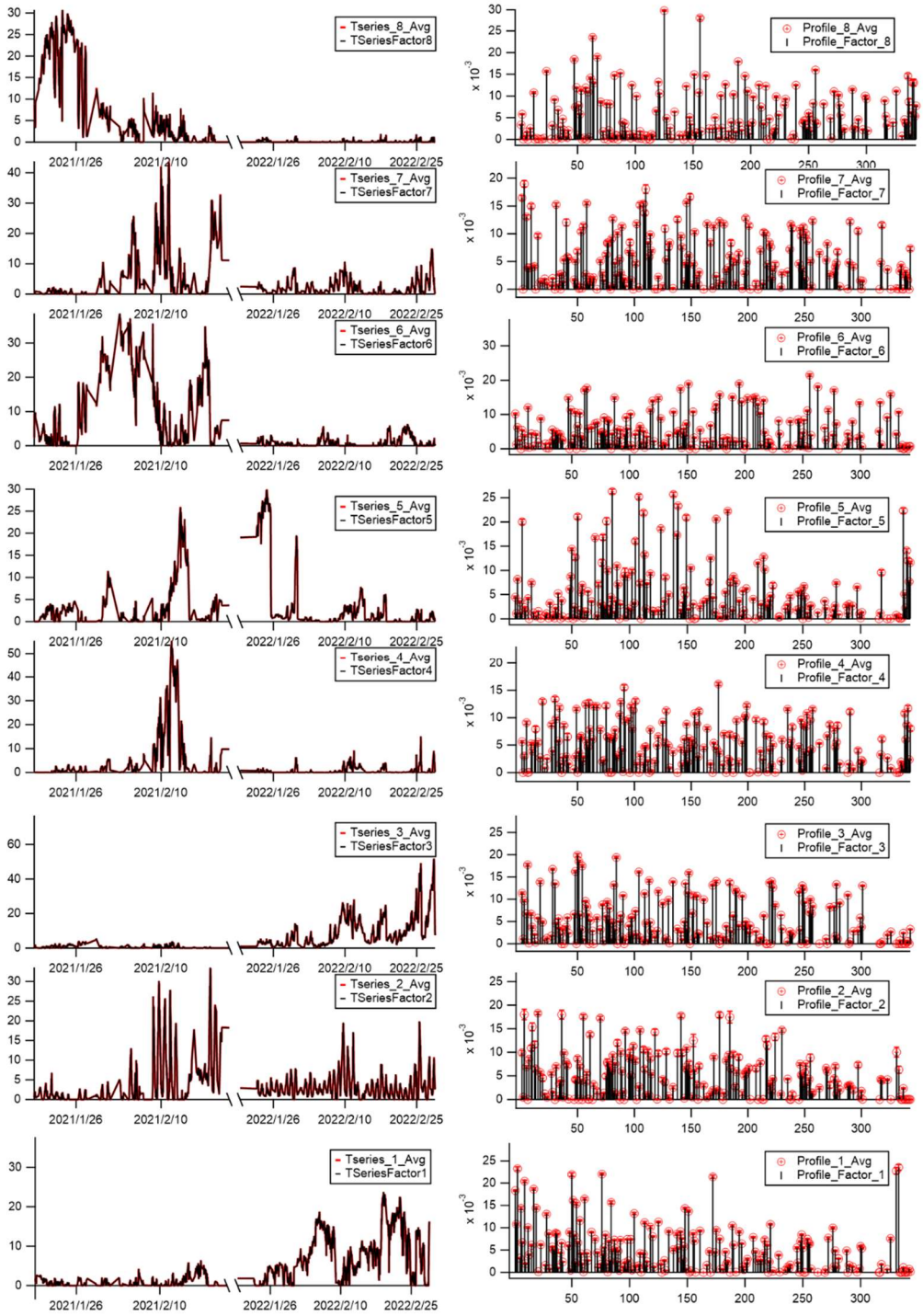


Figure S9. Temporal variations and mass spectra of eight factors from bootstrapping analysis (100 iterations) for PMF^2. The error bar is the standard deviation.

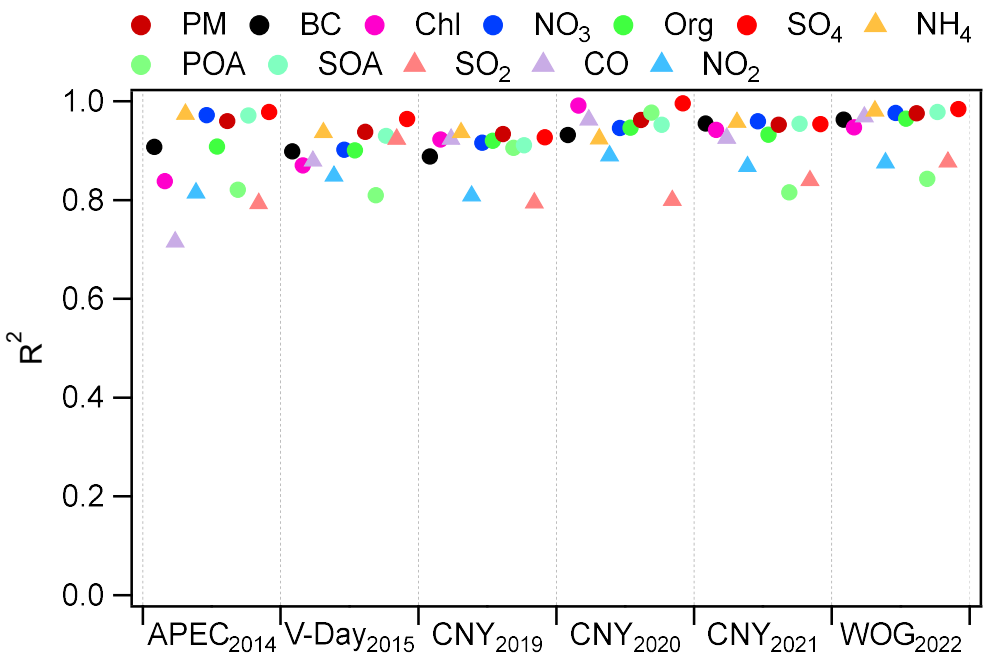


Figure S10. Correlation between results predicted by the Random Forest (RF) algorithm and observations.

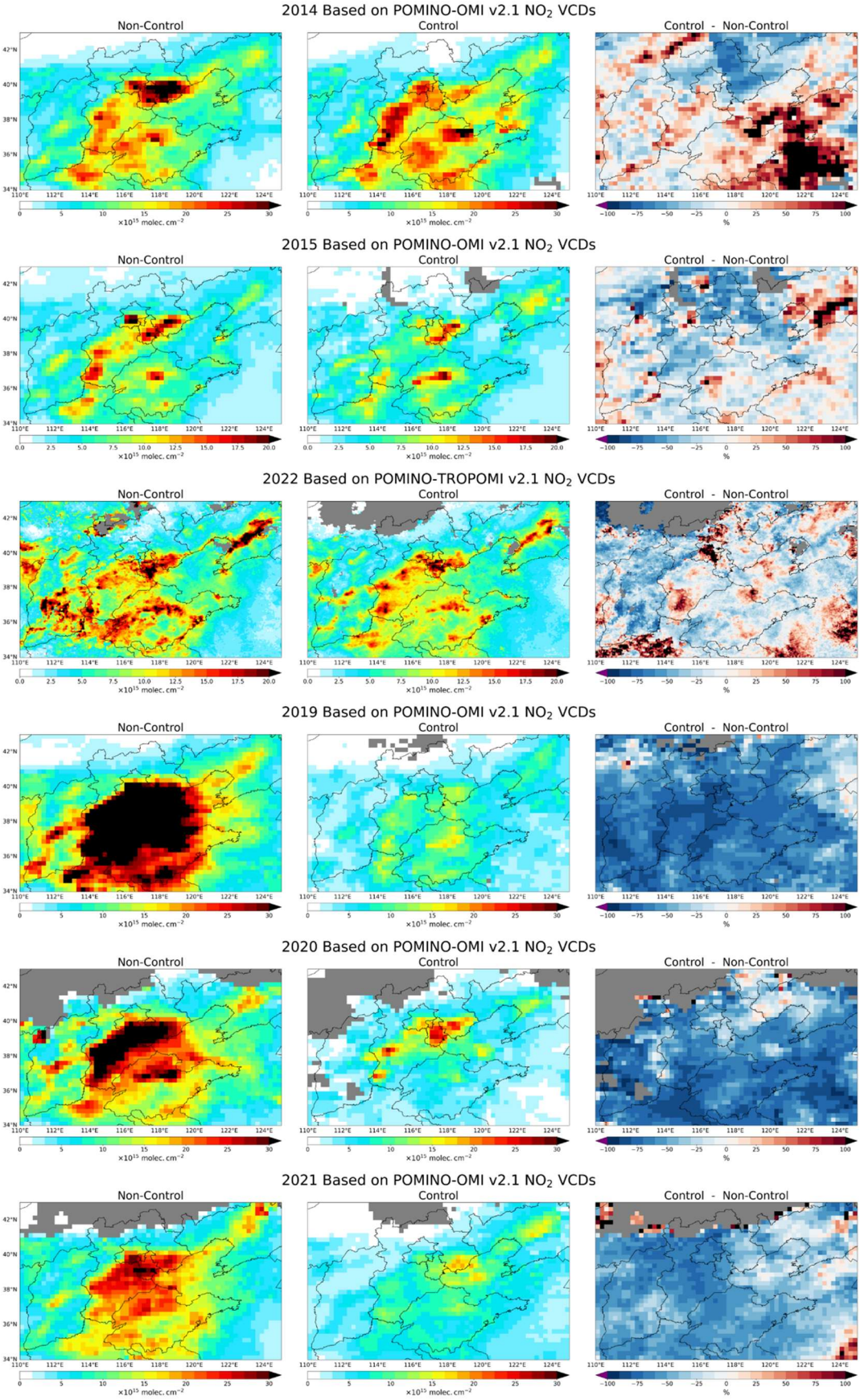

2014 Based on POMINO-OMI v2.1 NO2 VCDs
Non-Control
Control
Control - Non-Control
2015 Based on POMINO-OMI v2.1 NO2 VCDs
Non-Control
Control
Control - Non-Control
2022 Based on POMINO-TROPOMI v2.1 NO2 VCDs
Non-Control
Control
Control - Non-Control
2019 Based on POMINO-OMI v2.1 NO2 VCDs
Non-Control
Control
Control - Non-Control
2020 Based on POMINO-OMI v2.1 NO2 VCDs
Non-Control
Control
Control - Non-Control
2021 Based on POMINO-OMI v2.1 NO2 VCDs
Non-Control
Control
Control - Non-Control
×10^15 molec. cm^-2
%

Figure S11. Spatial distribution of tropospheric nitrogen dioxide vertical column densities (NO_2 VCDs) change rates (%) over the North China Plain. Results are derived from POMINO-OMI satellite retrievals and represent three policy interventions ($APEC_{2014}$, $V\text{-}Day_{2015}$, WOG_{2022}) and three Chinese New Year ($CNY_{2019\text{-}2021}$). Blue hues indicate decreases in NO_2 VCDs, while red hues represent increases.

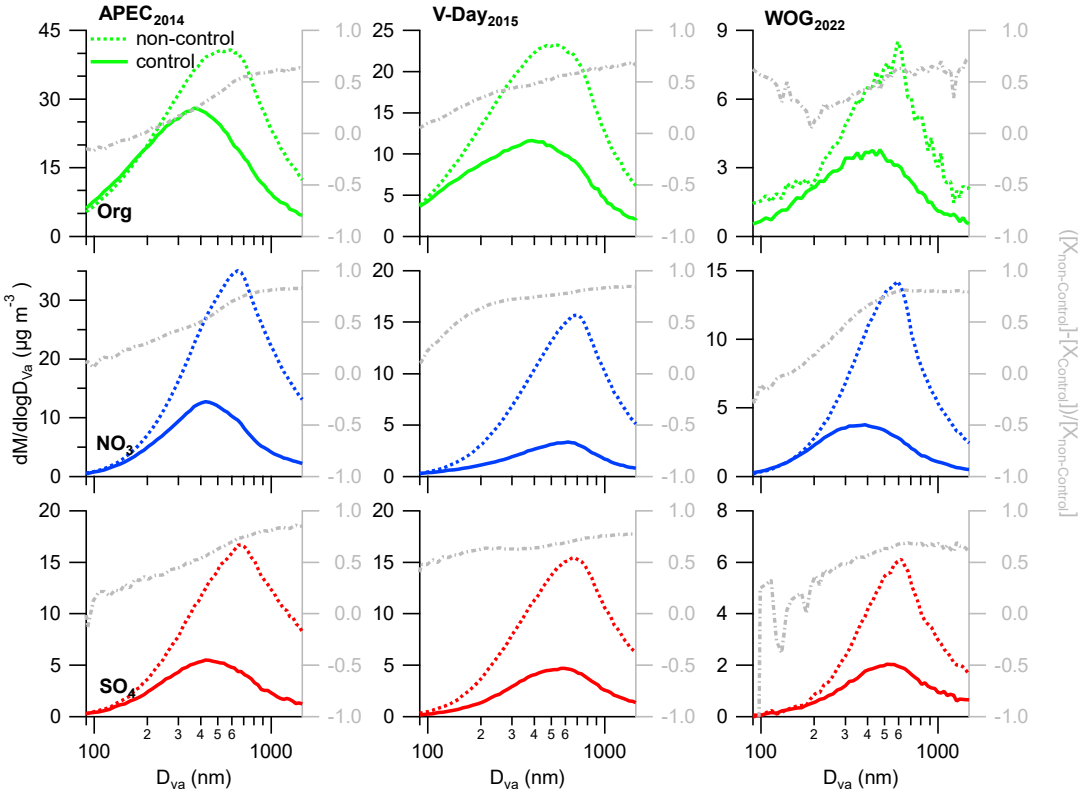


Figure S12. Average size distributions of sulfate, nitrate, and organics measured during emission variation and non-emission variation periods for regional coordinated emission reduction scenarios ($APEC_{2014}$, $V\text{-}Day_{2015}$, WOG_{2022}), also shown are the percentage changes in their mass concentrations across different size ranges.

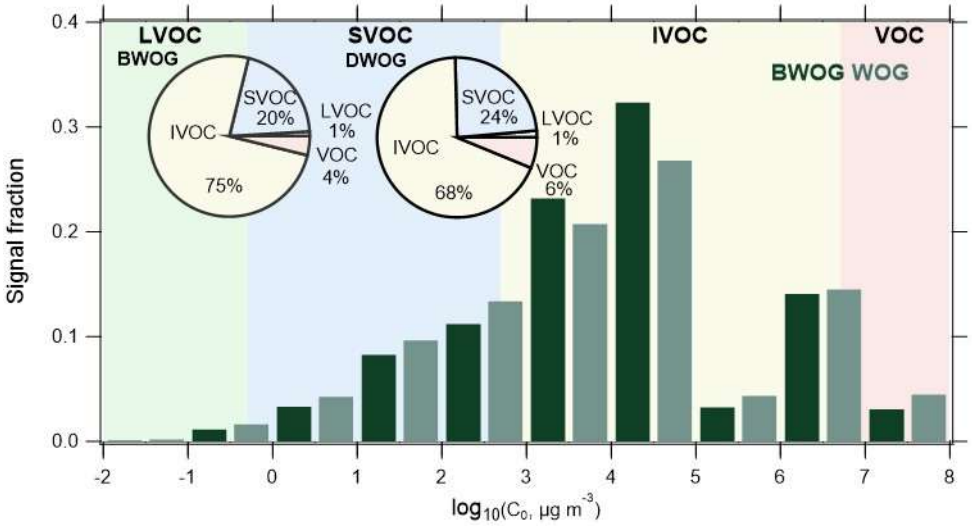


Figure S13. Signal fraction of VOC components at each saturation concentration before and during the Winter Olympic Games (BWOG and WOG).

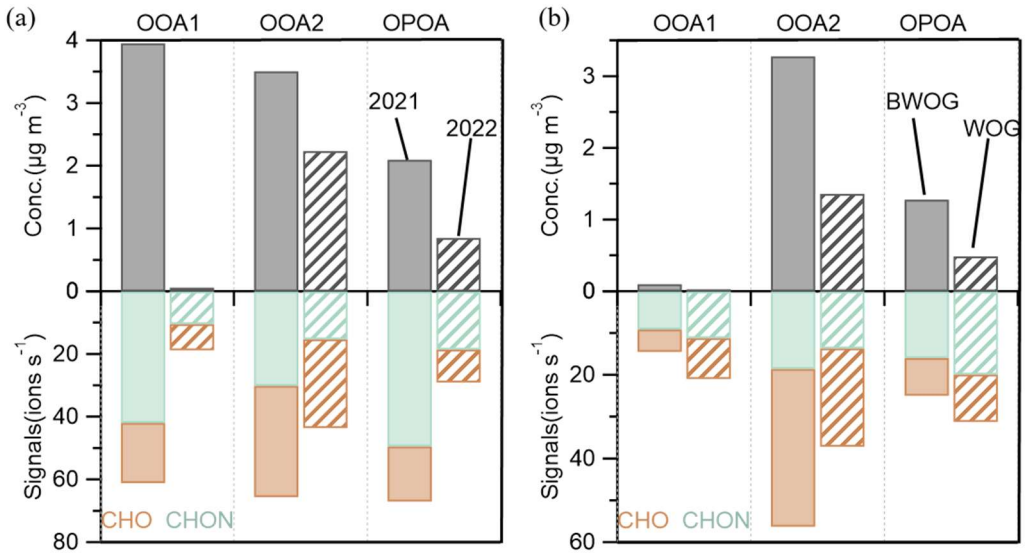


Figure S14. Mass concentrations of the three SOA factors in (a) 2021–2022, (b) BWOG–WOG, and signal intensities of CHO (orange) and CHON (green) compounds contributing to each factor.

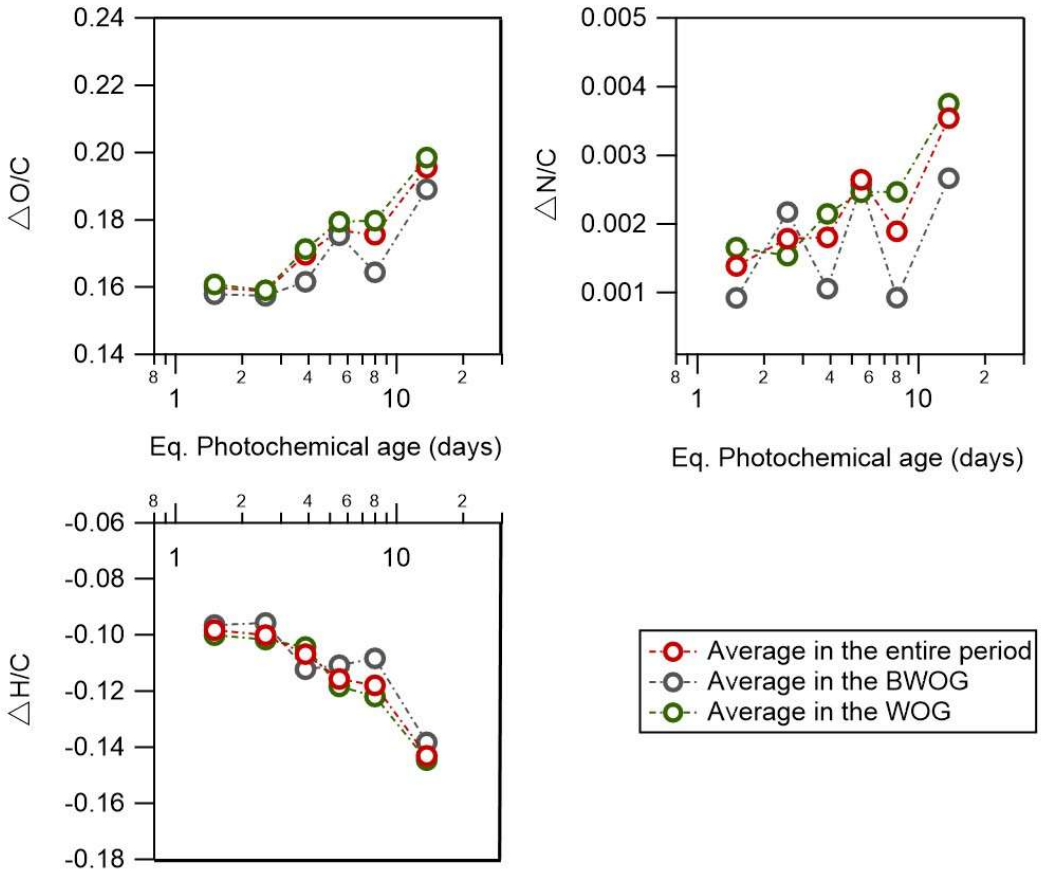


Figure S15. Absolute change of elemental ratios of OA as a function of photochemical age for BWOG, WOG, and entire period in 2022.

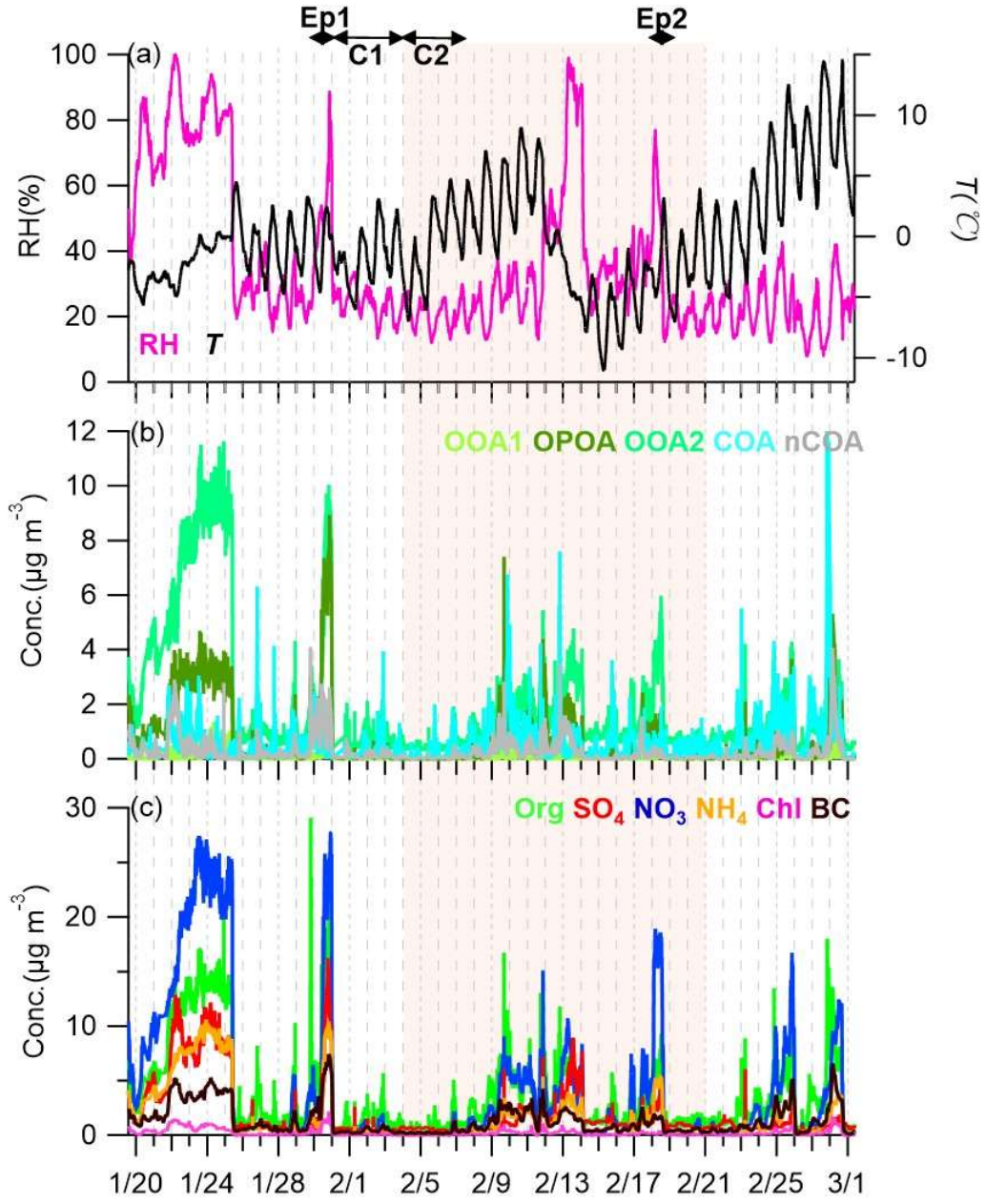


Figure S16. Time series of (a) relative humidity (RH) and temperature (*T*), mass concentrations of (b) OA factor and (c) NR-PM species in 2022. The shading area indicates WOG. Ep1 and Ep2 represent two pollution episodes and C1–C2 represent two cleaning episodes.

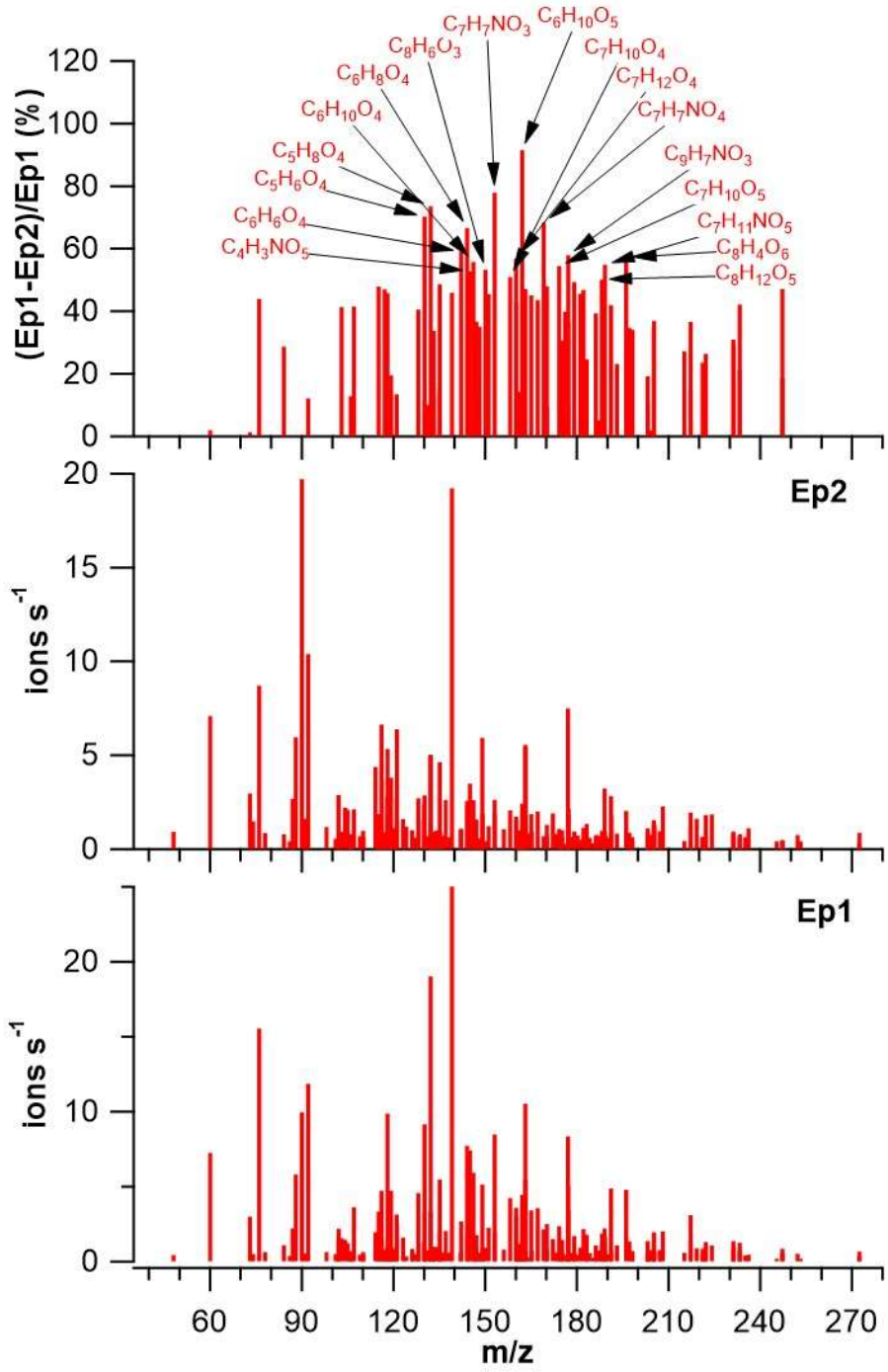


Figure S17. VOC mass spectra and relative changes between Ep1 and Ep2 Periods. Percentage reduction of individual VOC signals from Ep1 to Ep2 is calculated as (Ep1-Ep2)/Ep1 × 100%. Only positive values (indicating a reduction during Ep2) are displayed. Specific compounds with reductions exceeding 50% are labeled.

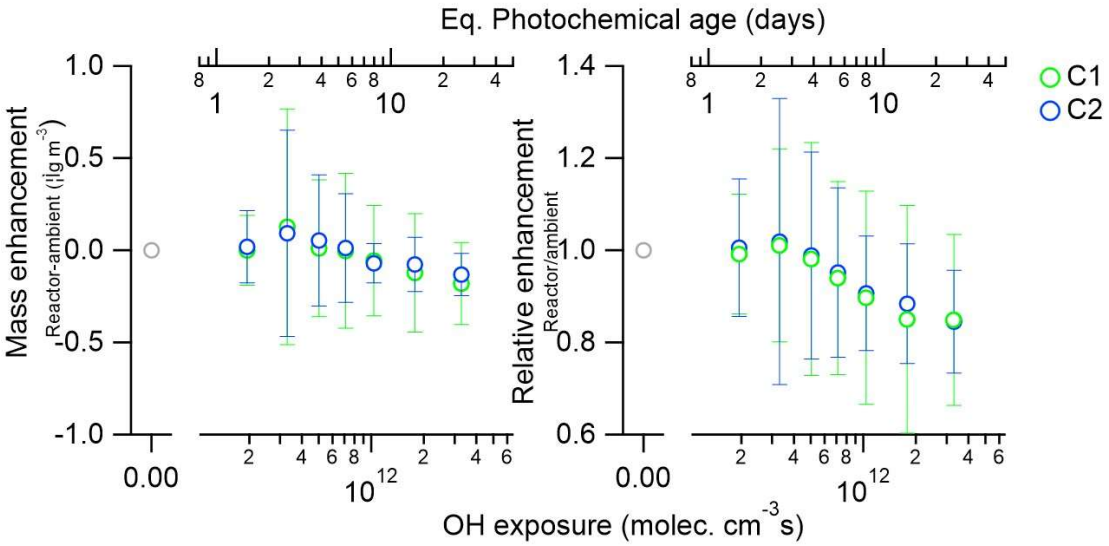


Figure S18. Absolute and relative enhancements of the mass concentration of OA as a function of photochemical age for C1 and C2 cleaning episodes.

Table S1. Overview of measurement campaigns, instrumentation, and defined analysis periods.

Event	Observation Period	NR-PM Instrument	BC Instrument	VOCs Instrument	Control / Non-Control Periods
$APEC_{2014}$	14 Oct – 12 Nov 2014	HR-ToF-AMS	AE22	—	**Control**: 3–12 Nov 2014 **Non-Control**: 14 Oct–3 Nov 2014
$V\text{-}Day_{2015}$	21 Aug – 24 Sep 2015	HR-ToF-AMS	AE22	—	**Control**: 21 Aug – 3 Sep 2015 **Non-Control**: 4–24 Sep 2015
CNY_{2019}	1 Jan – 14 Feb 2019	ToF-ACSM	AE33	—	**Control (CNY)**: 1–14 Feb 2019 **Non-Control (non-CNY)**: 1–31 Jan 2019
CNY_{2020}	20 Dec 2019 – 3 Feb 2020	ToF-ACSM	AE33	—	**Control (CNY)**: 21 Jan – 3 Feb 2020 **Non-Control (non-CNY)**: 20 Dec 2019 – 20 Jan 2020
CNY_{2021}	17 Jan – 21 Feb 2021	HR-ToF-AMS	AE33	ToF-CIMS	**Control (CNY)**: 8–21 Feb 2021 **Non-Control (non-CNY)**: 17 Jan – 7 Feb 2021
WOG_{2022}	19 Jan – 1 Mar 2022	HR-ToF-AMS	AE33	ToF-CIMS	**Control (WOG)**: 4–20 Feb 2022 **Non-Control (BWOG)**: 19 Jan – 3 Feb 2022
WOG_{2022}(Polluted Episodes)	19 Jan – 1 Mar 2022	HR-ToF-AMS	AE33	ToF-CIMS	**Ep2** (in WOG): 17–18 Feb 2022 **Ep1** (in BWOG): 30–31 Jan 2022

WOG_{2022}(Clean Episodes)	19 Jan – 1 Mar 2022	HR-ToF-AMS	AE33	ToF-CIMS	**C2** (in WOG): 4–7 Feb 2022 **C1** (in BWOG): 31 Jan – 3 Feb 2022

Table S2. Collection efficiency (CE) and relative ionization efficiency (RIE) used in 2014–2022.

Campaign	CE	RIEs				
		Org	SO_4	NO_3	Chl	NH_4
$APEC_{2014}$	0.5	1.4	1.2	1.1	1.3	5.0
$V\text{-}Day_{2015}$	0.5	1.4	1.2	1.1	1.3	5.0
CNY_{2019}	1	1.4	1.5	1.1	1.3	4.3
CNY_{2020}	1	1.4	1.0	1.1	1.3	3.1
CNY_{2021}	0.5	1.4	1.2	1.1	1.3	4.4
WOG_{2022}	0.5	1.4	1.3	1.1	1.3	5.3

Table S3. A summary of the OH exposure, eq. photochemical age, ozone (O_3) levels and O_3/OH_{exp} ratio for the different light intensities in the OFR reactor.

Light intensities (V)	OH exposure (molec cm^{-3} s)	Eq. days	O_3 Conc. (ppm)	O_3/OH_{exp} (ppm $molec^{-1}$ cm^3 s^{-1})
1.8	1.94×10^{11}	1.5	0.80±0.15	0.41×10^{-11}
1.9	3.31×10^{11}	2.6	1.02±0.17	0.31×10^{-11}
2.0	5.02×10^{11}	3.9	1.29±0.21	0.26×10^{-11}
2.1	7.18×10^{11}	5.5	1.57±0.24	0.22×10^{-11}
2.2	1.03×10^{12}	8.0	1.72±0.24	0.17×10^{-11}
3.0	1.83×10^{12}	13.7	3.30±0.35	0.18×10^{-11}

Table S4. Performance metrics of the random forest model used for meteorological normalization, including the root mean square error (RMSE) and mean absolute error (MAE) for each species and year.

		BC	Chl	NH_4	NO_2	NO_3	POA	SO_4	SOA
RMSE									
	$APEC_{2014}$	2.31	1.28	1.53	9.35	3.79	7.88	2.33	3.17
	$V\text{-}Day_{2015}$	0.71	0.26	1.60	7.13	3.48	2.52	1.91	2.25
	CNY_{2019}	0.95	1.61	3.01	7.70	3.30	1.66	2.91	2.61
	CNY_{2020}	0.60	1.30	2.23	4.85	3.06	0.98	1.90	2.05
	CNY_{2021}	0.49	0.45	1.44	5.07	3.53	1.52	1.46	2.02
	WOG_{2022}	0.29	0.08	0.36	2.14	1.14	0.41	0.33	0.54
MAE									
	$APEC_{2014}$	0.86	1.68	1.24	1.08	6.95	5.11	0.92	1.35
	$V\text{-}Day_{2015}$	0.46	0.15	1.00	5.04	1.87	1.63	1.24	1.62

CNY_{2019}	0.66	0.26	1.53	5.71	2.05	0.87	1.24	1.61
CNY_{2020}	0.40	0.47	1.16	3.62	1.85	0.57	0.94	1.18
CNY_{2021}	0.35	0.30	0.97	3.62	2.59	1.01	0.85	1.35
WOG_{2022}	0.20	0.05	0.21	1.62	0.76	0.27	0.20	0.36

Table S5. A summary of average mass concentrations of gaseous pollutants and particulate matter components measured during the emission variation and non-emission variation period for policy interventions ($APEC_{2014}$, $V\text{-}Day_{2015}$, WOG_{2022}) and population mobility ($CNY_{2019\text{-}2021}$).

Observation	Control period			non-Control period			CNY			non-CNY		
	$APEC_{2014}$	$V\text{-}Day_{2015}$	WOG_{2022}	$APEC_{2014}$	$V\text{-}Day_{2015}$	WOG_{2022}	2019	2020	2021	2019	2020	2021
Aerosol species ($\mu g/m^3$)												
NR-PM	40.0	17.4	7.8	80.2	46.8	19.9	23.6	37.2	47.2	27.8	20.1	39.5
BC	4.5	1.2	1.0	10.0	2.9	1.8	2.2	2.5	3.2	4.1	2.4	2.0
Org	22.1	10.2	2.7	32.9	19.5	5.6	10.5	16.2	16.0	13.6	7.9	12.5
NO_3	8.1	2.3	2.6	22.7	9.9	7.6	4.9	10.0	14.6	5.5	5.0	14.4
SO_4	3.9	3.3	1.4	11.7	10.7	3.3	4.0	4.9	7.4	4.1	3.7	5.6
NH_4	3.9	1.6	1.1	9.6	6.3	3.0	3.7	5.6	6.9	3.9	3.1	5.7
Chl	2.1	0.1	0.1	3.4	0.5	0.4	0.4	0.4	2.3	0.7	0.5	1.3

POA	13.0	3.7	0.7	15.8	6.2	0.8	2.4	1.3	3.7	4.6	1.8	3.8
SOA	6.8	7.1	1.9	18.7	13.2	4.6	8.1	14.5	11.3	8.7	5.9	8.7
Gaseous pollutants												
O_3(ppb)	13.4	37.7	26.4	8.4	36.8	20.0	20.9	25.5	19.4	13.7	12.3	13.2
NO_2(ppb)	30.0	15.7	11.7	47.9	34.0	15.0	15.4	18.7	21.9	29.9	27.4	23.7
SO_2(ppb)	3.6	0.9	0.8	4.5	2.5	0.9	2.7	3.3	2.0	3.8	2.5	1.6
CO(ppm)	0.8	0.6	0.4	1.2	0.9	0.6	0.7	0.9	0.9	0.9	0.8	0.7

Table S6. Summary of key VOCs identified in this study, including their molecular formulas, proposed identities, and supporting references.

Formula	compound assignments	proposed sources	Reference(s)
$C_5H_6O_4$	Dicarboxylic / peroxy acid	Biomass burning; biogenic VOC oxidation	(Leppla et al., 2026; Nguyen et al., 2011)
$C_6H_6O_4$	Oxygenated aromatic compound	Oxidation of anthropogenic aromatic VOCs	(Zheng et al., 2023)
$C_8H_{10}O_4$	Oxygenated aromatic compound	Aromatic VOC oxidation; biomass burning	(Molteni et al., 2018; Zhou et al., 2024)
$C_6H_5NO_3$	Nitrophenol	Aromatic VOC oxidation; biomass burning	(Ahmed et al., 2023; Zhou et al., 2024)
$C_7H_7NO_3$	Nitrophenol	Aromatic VOC oxidation; biomass burning	(Ahmed et al., 2023; Zhou et al., 2024)

$C_4H_6O_4$	dicarboxylic acid	Biomass burning	(Zhou et al., 2024)
$C_5H_8O_4$	Dicarboxylic acid	Biogenic VOC oxidation; biomass burning	(Ye et al., 2021; Zhou et al., 2024)
$C_6H_{10}O_4$	Dicarboxylic acid	Biogenic VOC oxidation; biomass burning	(Ye et al., 2021; Zhou et al., 2024)
$C_7H_{12}O_4$	dicarboxylic acid	Biomass burning	(Mochida et al., 2003; Zhou et al., 2024)
$C_5H_9NO_4$	Organic nitrate	Biogenic VOC oxidation	(Lee et al., 2014)
$C_5H_9NO_5$	Organic nitrate	Biogenic VOC oxidation	(Wu et al., 2021)
$C_5H_9NO_6$	Organic nitrate	Biogenic VOC oxidation	(Wu et al., 2021)
$C_8H_{10}O_5$	Oxygenated aromatic	Oxidation of biogenic VOCs ; anthropogenic aromatic VOCs	(Jiang et al., 2025; Molteni et al., 2018)
$C_7H_{10}O_5$	Oxygenated aromatic compound	Oxidation of anthropogenic aromatic VOCs	(Molteni et al., 2018)
$C_7H_7NO_4$	Nitrophenol	Biomass burning	(Iinuma et al., 2010; Zhou et al., 2024)

Table S7. A summary of average signal intensities and signal fractions of different VOC components for WOG_{2022} and the same period in 2021, BWOG, WOG , and Ep1, Ep2 pollution episodes, C1, C2 cleaning episodes in WOG_{2022}.

	BWOG	WOG	Ep1	Ep2	C1	C2	2021	2022
Total signals (ions s^{-1})	253.5	266.4	407.9	340.3	152.5	210.0	456.9	261.7
SVOC signals (ions s^{-1})	51.1	63.8	100.2	82.5	35.0	46.0	138.4	59.9

IVOC signals (ions s^{-1})	189.9	182.0	289.1	235.2	105.7	144.8	293.3	186.6
CHO signals (ions s^{-1})	147.6	150.9	202.5	176.0	92.6	135.6	194.9	149.7
CHON signals (ions s^{-1})	105.9	115.5	205.4	164.3	59.9	74.3	262.1	112.1
IVOC Proportion (%)	74.9	68.3	70.9	69.1	69.3	69.0	64.2	71.3
SVOC proportion (%)	20.2	23.9	24.6	24.2	33.2	31.7	30.3	22.9
CHO(%)	58.2	56.6	49.6	51.7	60.7	64.6	42.6	57.2
CHON(%)	41.8	43.4	50.4	48.3	39.3	35.4	57.4	42.8

References

Ahmed, M., Rappenglueck, B., Ganranoo, L., Dasgupta, P.K., 2023. Source apportionment of gaseous Nitrophenols and their contribution to HONO formation in an urban area. Chemosphere 338, 139499.

Canonaco, F., Crippa, M., Slowik, J.G., Baltensperger, U., Prévôt, A.S.H., 2013. SoFi, an IGOR-based interface for the efficient use of the generalized multilinear engine (ME-2) for the source apportionment: ME-2 application to aerosol mass spectrometer data. Atmospheric Measurement Techniques 6, 3649-3661.

Cubison, M.J., Ortega, A.M., Hayes, P.L., Farmer, D.K., Day, D., Lechner, M.J., Brune, W.H., Apel, E., Diskin, G.S., Fisher, J.A., Fuelberg, H.E., Hecobian, A., Knapp, D.J., Mikoviny, T., Riemer, D., Sachse, G.W., Sessions, W., Weber, R.J., Weinheimer, A.J., Wisthaler, A., Jimenez, J.L., 2011. Effects of aging on organic aerosol from open biomass burning smoke in aircraft and laboratory studies. Atmospheric Chemistry and Physics 11, 12049-12064.

Donahue, N.M., Robinson, A.L., O, S.C., N, P.S., 2006. Coupled Partitioning, Dilution, and Chemical Aging of Semivolatile Organics. Environmental Science & Technology 40, 2635-2643.

Fröhlich, R., Crenn, V., Setyan, A., Belis, C.A., Canonaco, F., Favez, O., Riffault, V., Slowik, J.G., Aas, W., Aijälä, M., Alastuey, A., Artiñano, B., Bonnaire, N., Bozzetti, C., Bressi, M., Carbone, C., Coz, E., Croteau, P.L., Cubison, M.J., Esser-Gietl, J.K., Green, D.C., Gros, V., Heikkinen, L., Herrmann, H., Jayne, J.T., Lunder, C.R., Minguillón, M.C., Močnik, G., O'Dowd, C.D., Ovadnevaite, J., Petralia, E., Poulain, L., Priestman, M., Ripoll, A., Sarda-Estève, R., Wiedensohler, A., Baltensperger, U., Sciare, J., Prévôt, A.S.H., 2015. ACTRIS ACSM intercomparison – Part 2: Intercomparison of ME-2 organic source apportionment results from 15 individual, co-located aerosol mass spectrometers. Atmospheric Measurement Techniques 8, 2555-2576.

Iinuma, Y., Böge, O., Gräfe, R., Herrmann, H., 2010. Methyl-Nitrocatechols: Atmospheric Tracer Compounds for Biomass Burning Secondary Organic Aerosols. Environmental Science & Technology 44, 8453-8459.

Jiang, H., Deng, Y., Huo, Y., Wang, F., Chen, Y., Guo, H., 2025. Measurement report: Molecular insights into organic aerosol sources and formation at a regional background site in South China. Atmospheric Chemistry and Physics 25, 13711-13727.

Lanz, V.A., Alfarra, M.R., Baltensperger, U., Buchmann, B., Hueglin, C., Prévôt, A.S.H., 2007. Source apportionment of submicron organic aerosols at an urban site by factor analytical modelling of aerosol mass spectra. Atmospheric Chemistry and Physics 7, 1503-1522.

Lee, B.H., Lopez-Hilfiker, F.D., Mohr, C., Kurtén, T., Worsnop, D.R., Thornton, J.A., 2014. An Iodide-Adduct High-Resolution Time-of-Flight Chemical-Ionization Mass Spectrometer: Application to Atmospheric Inorganic and Organic Compounds. Environmental Science & Technology 48, 6309-6317.

Leppla, D., Hildmann, S., Zannoni, N., Kremper, L.A., Holanda, B.A., Williams, J., Pöhlker, C., Wolff, S., Sà, M., Solci, M.C., Pöschl, U., Hoffmann, T., 2026.

Comprehensive non-targeted molecular characterization of organic aerosols in the Amazon rainforest. Atmospheric Chemistry and Physics 26, 365-390.

Li, Y., Poeschl, U., Shiraiwa, M., 2016. Molecular corridors and parameterizations of volatility in the chemical evolution of organic aerosols. Atmospheric Chemistry and Physics 16, 3327-3344.

Mochida, M., Kawabata, A., Kawamura, K., Hatsushika, H., Yamazaki, K., 2003. Seasonal variation and origins of dicarboxylic acids in the marine atmosphere over the western North Pacific. Journal of Geophysical Research: Atmospheres 108.

Molteni, U., Bianchi, F., Klein, F., El Haddad, I., Frege, C., Rossi, M.J., Dommen, J., Baltensperger, U., 2018. Formation of highly oxygenated organic molecules from aromatic compounds. Atmospheric Chemistry and Physics 18, 1909-1921.

Nguyen, T.B., Roach, P.J., Laskin, J., Laskin, A., Nizkorodov, S.A., 2011. Effect of humidity on the composition of isoprene photooxidation secondary organic aerosol. Atmospheric Chemistry and Physics 11, 6931-6944.

Paatero, P., Hopke, P.K., 2009. Rotational Tools for Factor Analytic Models. Journal of Chemometrics 23, 91-100.

Petit, J.E., Favez, O., Sciare, J., Canonaco, F., Croteau, P., Močnik, G., Jayne, J., Worsnop, D., Leoz-Garziandia, E., 2014. Submicron aerosol source apportionment of wintertime pollution in Paris, France by double positive matrix factorization (PMF2) using an aerosol chemical speciation monitor (ACSM) and a multi-wavelength Aethalometer. Atmospheric Chemistry and Physics 14, 13773-13787.

Sun, Y.L., Jiang, Q., Xu, Y.S., Ma, Y., Zhang, Y.J., Liu, X.G., Li, W.J., Wang, F., Li, J., Wang, P.C., Li, Z.Q., 2016. Aerosol characterization over the North China Plain: Haze life cycle and biomass burning impacts in summer. Journal of Geophysical Research-Atmospheres 121, 2508-2521.

Sun, Y.L., Wang, Z.F., Fu, P.Q., Yang, T., Jiang, Q., Dong, H.B., Li, J., Jia, J.J., 2013. Aerosol composition, sources and processes during wintertime in Beijing, China. Atmospheric Chemistry and Physics 13, 4577-4592.

Wu, R., Vereecken, L., Tsiligiannis, E., Kang, S., Albrecht, S.R., Hantschke, L., Zhao, D., Novelli, A., Fuchs, H., Tillmann, R., Hohaus, T., Carlsson, P.T.M., Shenolikar, J., Bernard, F., Crowley, J.N., Fry, J.L., Brownwood, B., Thornton, J.A., Brown, S.S., Kiendler-Scharr, A., Wahner, A., Hallquist, M., Mentel, T.F., 2021. Molecular composition and volatility of multi-generation products formed from isoprene oxidation by nitrate radical. Atmospheric Chemistry and Physics 21, 10799-10824.

Ye, C.S., Yuan, B., Lin, Y., Wang, Z.L., Hu, W.W., Li, T.G., Chen, W., Wu, C.H., Wang, C.M., Huang, S., Qi, J.P., Wang, B.L., Wang, C., Song, W., Wang, X.M., Zheng, E., Krechmer, J.E., Ye, P.L., Zhang, Z.Y., Wang, X.M., Worsnop, D.R., Shao, M., 2021. Chemical characterization of oxygenated organic compounds in the gas phase and particle phase using iodide CIMS with FIGAERO in urban air. Atmospheric Chemistry and Physics 21, 8455-8478.

Zheng, P., Chen, Y., Wang, Z., Liu, Y., Pu, W., Yu, C., Xia, M., Xu, Y., Guo, J., Guo, Y., Tian, L., Qiao, X., Huang, D.D., Yan, C., Nie, W., Worsnop, D.R., Lee, S., Wang, T., 2023. Molecular Characterization of Oxygenated Organic Molecules and Their Dominating Roles in Particle Growth in Hong Kong. Environ Sci Technol 57,

7764-7776.
Zhou, W., Xu, W.Q., Li, Z.J., Lei, L., Li, Y., Sun, J.X., Du, A.D., Zhang, Z.Q., Li, Y., Fu, P.Q., Ge, X.L., Sun, Y.L., 2024. Molecular Characterization of Gaseous Organic Acids and Nitrogen-Containing Compounds From Crop Straw and Wood Burning. Journal of Geophysical Research-Atmospheres 129, e2023JD040568.